Expert Systems With Applications 200 (2022) 116883

Contents lists available at ScienceDirect

Expert Systems With Applications

journal homepage: www.elsevier.com/locate/eswa

External force estimation and disturbance rejection for Micro Aerial Vehicles☆

Andreas Papadimitriou [a,*], Hedyeh Jafari [a], Sina Sharif Mansouri [b], George Nikolakopoulos [a]

[a] Robotics & AI Team, Department of Computer, Electrical and Space Engineering, Luleå University of Technology, Luleå SE-97187, Sweden
[b] Research and Development Engineer at the Autonomous Driving Lab in Scania Group, Sweden

ARTICLE INFO

Keywords:
External disturbances
Non Linear Moving Horizon Estimation
Non linear Model Predictive Control

ABSTRACT

To deploy Micro Aerial Vehicles (MAVs) in real-world applications, there is a need for online methods to cope with uncertainties in localization and external disturbances. In this article, we propose a set of novel real-time embedded Nonlinear Model Predictive Control (NMPC) and Nonlinear Moving Horizon Estimation (NMHE) modules for MAV based external disturbance rejection. The NMPC and NMHE are based on the dynamic model of the MAV, thus, avoiding the need for system identification and creating specific aerodynamic models, a benefit that results in a generic solution capable of being independent of the type of the MAVs. As it will be presented, the NMHE estimates the external forces, while the NMPC generates thrust and attitude commands for the low-level controller to compensate the various disturbances that could occur, such as wind gusts, tethered payload, and varying center of gravity. The proposed method is evaluated extensively in multiple experimental results that include the scenarios of position hold against an actuating wind-wall, adding payload, and changing the MAV's arm configurations.

1. Introduction

Recent technological advancements in MAVs have resulted to their deployment in real-world applications, such as infrastructure inspection (Mansouri, Kanellakis, Fresk, Kominiak, & Nikolakopoulos, 2018), aerial terrain mapping (Mansouri, Kanellakis, Georgoulas, et al., 2018), underground mine inspection (Mansouri, Kanellakis, Kominiak, & Nikolakopoulos, 2020; Mansouri, Karvelis, Kanellakis, Kominiak, & Nikolakopoulos, 2019), search-and-rescue missions (Sampedro et al., 2018), physical interaction with environment (Wuthier et al., 2016), aerial payload and transportation (Pereira & Dimarogonas, 2019). In these applications, undesired disturbances, such as wind gusts, turbulences, or external forces in interaction with the environment are inevitable. In addition, the lack of consideration for these external disturbances from the MAV's control schemes affect the overall mission performance and results in an increased risk of collision and overall failure of the mission (Belcastro et al., 2017).

In an attempt to robustify Micro Aerial Vehicles (MAVs) against unwanted external disturbances, this article proposes a novel online embedded Nonlinear Moving Horizon Estimation (NMHE) and Nonlinear Model Predictive Control (NMPC) frameworks. The proposed method can estimate the external disturbances while considering the nonlinear dynamics of the MAV, without requiring the platform's system identification. Furthermore, the NMHE estimates the external forces, without relying on external sensors installed either onboard the aerial platform or on the environment, such as weather station measurements or force sensors. Contrary, our method feeds the estimated forces to an enhanced position NMPC controller that provides disturbance-compensated thrust and attitude commands to the low-level controller, which regulates the platform's motor commands. In the proposed framework, the NMHE and NMPC optimization problems are solved online by the utilization of Proximal Averaged Newton-type method for Optimal Control (PANOC) (Sathya et al., 2018; Sopasakis, Fresk, & Patrinos, 2020) that is a fast solver for nonlinear optimal control problems and guarantees real-time performance, a key component for embedded applications. Finally, both developed modules are evaluated in different experimental scenarios with different platforms, while none of the experiments result in any collision.

☆ This work has been partially funded by the European Unions Horizon 2020 Research and Innovation Programme under the Grant Agreement No. 869379 illuMINEation.

* Corresponding author.
E-mail addresses: andpap@ltu.se (A. Papadimitriou), hedjaf@ltu.se (H. Jafari), sina.sharif.mansouri@scania.com (S.S. Mansouri), geonik@ltu.se (G. Nikolakopoulos).

https://doi.org/10.1016/j.eswa.2022.116883
Received 3 May 2021; Received in revised form 11 January 2022; Accepted 10 March 2022
Available online 24 March 2022

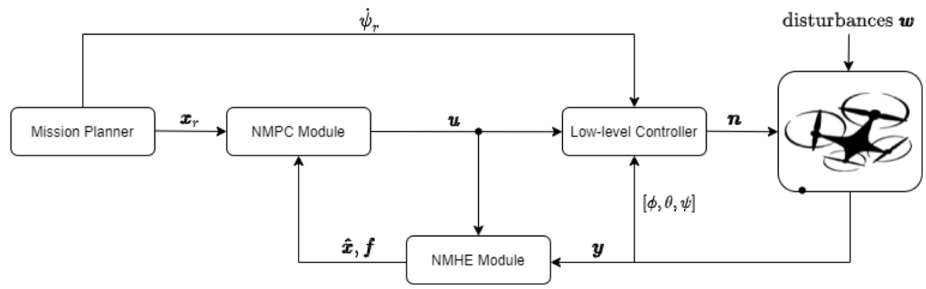

Fig. 1. Block diagram of the proposed NMPC and NMHE framework. A high-level controller or mission planner provides the reference, and the NMPC generates the related thrust and attitude commands based on the state estimates and external forces. Lastly, the low-level controller generates the motor commands for the MAV.

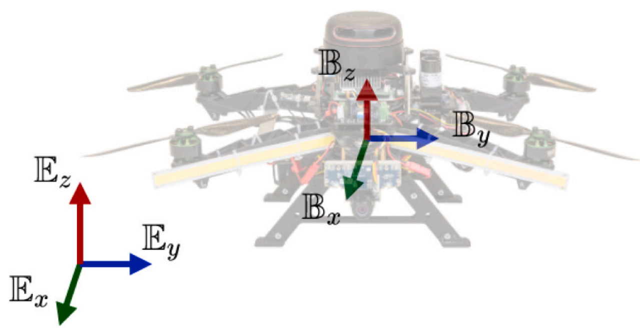

Fig. 2. MAV with the attached body fixed frame $\mathbb{B}$ and inertial frame $\mathbb{E}$.

1.1. Background & motivation

The majority of research studies focus on improving the flight performance of a MAV by reckoning external forces and wind velocity to enhance the state estimates and compensate for any disturbances. A common approach to acquiring wind velocity is to utilize sensors, such as anemometers or airspeed sensors that can measure the surrounding environmental conditions (Hollenbeck, Nunez, Christensen, & Chen, 2018; Wolf et al., 2017). However, the physical sensors are sensitive to disturbances generated from turbulence generated by the MAV's propellers in the form of corrupting noise. In contrast, the installation of extra physical components increases the platform's overall weight with a direct reduction of the corresponding flight time.

In the related literature, many studies consider the problem of wind estimation based on on-board sensor suites, such as Inertial Measurement Unit (IMU) and Global Positioning System (GPS). As a characteristic example, the authors in Cho, Kim, Lee, and Kee (2011) proposed an Extended Kalman Filter (EKF) with a GPS and pitot tube to estimate the wind speed and direction. In Neumann and Bartholmai (2015) the authors utilized the already available MAV's sensors, like the IMU and the GPS, to acquire estimates of the wind state. In contrast to the previous approaches, the proposed novel methodology estimates the speed and direction of the wind, based on the on-board sensors and global information from GPS, while the overall performance of the method is evaluated in a wind tunnel and during extended field tests. Nevertheless, both methods rely on the body and global velocities for obtaining wind velocity equations.

In the related literature, many studies consider the problem of wind estimation based on on-board sensor suites, such as IMU and GPS. As a characteristic example, the authors in Cho et al. (2011) proposed an EKF with a GPS and pitot tube to estimate the wind speed and direction. In Neumann and Bartholmai (2015) the authors utilized the already available MAV's sensors, like the IMU and the GPS, to acquire estimates of the wind state. In contrast to the previous approaches, the proposed novel methodology estimates the speed and direction of the wind, based on the on-board sensors and global information from GPS, while the overall performance of the method is evaluated in a wind tunnel and during extended field tests. Nevertheless, both methods rely on the body and global velocities for obtaining wind velocity equations.

Lately, NMHE methods are also getting more attention (Haseltine & Rawlings, 2005) for their ability to estimate complex nonlinear dynamic models while they can handle inequality constraints. In Wenz and Johansen (2017), the authors proposed a wind estimation framework based on the kinematic model via Moving Horizon Estimation (MHE). The method relies on IMU, pitot-static tube, and GPS that limits the usage of that method in GPS denied environments, like subterranean environments. In general, there have been few works that study the use of MHE for target tracking of MAV, like in Quintero, Copp, and Hespanha (2015) that proposed a MHE based on dynamic of the MAV for target tracking, while the target has a constant velocity or it became evasive, while the method was validated through simulations. However, the problem formulation is different from the wind estimation, and the target tracking is vision-based and depends on pixel coordinates.

In Hentzen, Stastny, Siegwart, and Brockers (2019), an EKF and an Unscented Kalman Filter (UKF) disturbance estimator is tested for the position control and disturbance rejection of a multirotor. The performance of this framework is evaluated under wind-wall and ground effect experiments. The external forces are modeled as random Gaussian walk and included in the MAV dynamics, while the position control lacks tuning discussion and adaptive weight tuning parameters. To compensate for rotor failures in-flight, the authors of Sun and de Visser (2019) developed a parametric model of the residual forces, while the developed model has been tested under the effect of rotor failures. In Kan et al. (2019) the authors presented a polynomial methodology for analyzing the ground effect of MAV and the produced thrust. In Kocer, Tiryaki, Pratama, Tjahjowidodo, and Seet (2019), to compensate for the turbulence effects, while a MAV flying in close proximity to the ceiling, the external forces were modeled as constant and estimated using a MHE, while in the sequel, the estimated forces were added as augmented states in the dynamics of the system. It should also be noted at this point that all the studies above did not provide a related discussion about compensating for the center of gravity variations or additive payload, while Table 1 provides an overview of state-of-art on external force estimation and rejection.

In contrast to the studies in Table 1, it will be presented in the sequel that our method outperforms for external forces generated from various sources and for different platforms. The main limitation of all the studies, including this one, is reliable odometry information. Thus all of these approaches were tested with the utilization of a Motion Capture (Mo-Cap) system. In addition, we show successful estimation and good disturbance rejection in simulation when the states are corrupted by extreme noise, which would be the equivalent of poor odometry information.

1.2. Contributions

The first contribution stems from the formulation of the NMHE and the NMPC modules. The developed NMHE reckons external disturbance

Table 1
State-of-art external disturbance estimation and rejection.

References	Method	Sensors	Evaluation	Computation time	Pros/Cons
(Hentzen et al., 2019)	NMPC + EKF NMPC + UKF	IMU Requires odometry	High Power Fan	NMPC 4ms EKF 8ms UKF 20ms	Rely only in position and orientation measurements.
(Kan et al., 2019)	Data-driven polynomial models	IMU Requires odometry	Flights in close proximity to ground in Lab environment	Models are designed offline. Not available	Only for overcoming ground effect during near ground flights
(Sun & de Visser, 2019)	Parametric force and moment models	IMU Requires odometry	Large scale wind tunnel	Identification is completed offline. Not available	Requires system identification, thus data collection is required prior to the design of the controller.
(Kocer et al., 2019)	NMPC + NMHE	IMU Requires odometry	Flights in close proximity to ceiling in lab environment	NMPC 1.8 ms NMHE 3.4 ms	Compensates for vertical forces in close ceiling flights

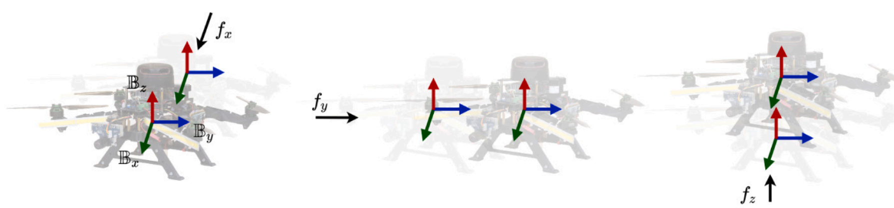

Fig. 3. Schematic illustrating the effect of the external forces on the MAV body frame axes. The f_x, f_y, f_z results to the displacement of the MAV in the x, y, z body axes, respectively.

forces, while the NMPC compensates for these external disturbances through properly adjusted thrust and attitude commands. The overall proposed framework is solved by PANOC, which guarantees real-time performance and it is suitable for embedded computers. Moreover, the proposed methodology compensates for external disturbances, independent of their source or without the need for additional on-board or environmental sensorial information.

The second contribution is the general formulation of the NMPC and NMHE, which makes them suitable for any MAV platform and independent of the aerodynamic model and without relying on system identification techniques. In addition, in the proposed formulation, there are no modifications on the MAV's low-level controller, while the position NMPC controller compensates for the estimated external forces.

The third and final contribution stems from the extensive evaluation of the proposed method in four experimental scenarios. Initially, while trying to maintain position, the platform is subject to strong winds reaching up to 7.5 [m/s] generated from a wind tunnel fan. In the second scenario, the MAV is commanded to hold the position, while the wind is created from a wind-wall that is able to produce winds of variable velocity, and the platform is tested in the range of 0 [m/s] to 12 [m/s]. In the third scenario, the MAV is evaluated for compensating the effect of a pendulum during flight. In this case, a tethered payload is let to swing under the platform, resulting in the application of varying forces in terms of amplitude and frequency. The NMHE and NMPC modules estimate and compensate, respectively. In the final scenario, the overall framework is experimentally evaluated for compensating the center of gravity and other aerodynamic effects of a re-configurable MAV subject to in-flight structural re-formations. The re-configurable MAV can fold its arms individually around its main body resulting even in non-symmetric morphology (Papadimitriou, Mansouri, Kanellakis, & Nikolakopoulos, 2021). In this case, the low-level controller of the re-configurable MAV does not account for these dynamic variations. Thus the NMHE estimates them as forces that are compensated through the NMPC module.

The following link https://youtu.be/u6gQuL-oqWY provides a video summary of the experimental evaluation.

1.3. Outline

The rest of this article is structured as follows. Initially, the utilized notations are introduced in Section 2, while, the MAV dynamics are presented in Section 3. The formulation of the NMPC and the NMHE are presented in Sections 4 and 5, respectively. Section 6 presents the experimental set-ups, tuning parameters, and the extensive simulation and experimental evaluation of the proposed framework. Finally, the concluding remarks are given in Section 7 summarizing our findings while providing related future research directions that could further improve the current novel established framework

2. Notation and preliminaries

A vector in $\mathbb{R}^n$ is predetermined as a column vector in $\mathbb{R}^{n\times 1}$. The identity matrix in $\mathbb{R}^{n\times n}$ is denoted by $\mathbf{I}_n$. The $\|\cdot\|$ represents the norm two for vectors. The *state* and *input* vectors in the NMPC formulation are $\boldsymbol{x}$ and $\boldsymbol{u}$, respectively. The estimated state and the force vector are denoted by $\hat{\boldsymbol{x}}$ and $\boldsymbol{f}$, respectively, while the augmented state for the NMHE is $\bar{\boldsymbol{x}} = [\boldsymbol{x}, \boldsymbol{f}]^\top$. The position vector is $\boldsymbol{p}$ and the linear velocities vector is $\boldsymbol{v}$, while ϕ and θ are the roll and pitch angles of the platform. Fig. 1 depicts the block diagram of the proposed structure with the high-level NMPC controller, the NMHE as the state and external force estimator and the low-level controller with the MAV in the loop.

The NMPC module (presented in Section 4) generates the control actions $\boldsymbol{u}$ for navigating to the reference waypoint $\boldsymbol{x}_r$, based on the estimated states $\hat{\boldsymbol{x}}$ and the estimated external forces $\boldsymbol{f}$ from the NMHE (presented in Section 5). For tracking the desired roll and pitch angles, as well as to regulate the altitude and heading of the MAV a low-level controller is incorporated. By utilizing the data from the IMU of the flight controller, the resulting feedback law of the low-level control is in the form of a PD-controller that generates thrust T and torques τ_x, τ_y, and τ_z. Torques and thrust commands are converted properly in the sequel to motor commands based on the platform requirements $\boldsymbol{n} \in R^m$, where m is the number of motors of the platform (Jackson, Ellingson, & McLain, 2016).

3. MAV dynamics

The MAV is considered as a six Degree of Freedom (DoF) object with a Body-Fixed Frame $\mathbb{B}$ attached and the inertial frame $\mathbb{E}$, as depicted in Fig. 2. The MAV is modeled by the position of the center of mass in the inertia frame and the orientation of the body around each axes with respect to the inertial frame (Kamel, Stastny, Alexis, & Siegwart, 2017; Mansouri, Kanellakis, Lindqvist, et al., 2020). The MAV dynamics are defined in the body frame and modeled by (1) as:

$$\dot{\boldsymbol{p}}(t) = \boldsymbol{v}(t) \tag{1a}$$

$$\dot{\boldsymbol{v}}(t) = \boldsymbol{R}_{x,y}(\theta,\phi)\begin{bmatrix}0\\0\\T\end{bmatrix} + \begin{bmatrix}0\\0\\-g\end{bmatrix} - \begin{bmatrix}A_x & 0 & 0\\0 & A_y & 0\\0 & 0 & A_z\end{bmatrix}\boldsymbol{v}(t) + \boldsymbol{f}(t), \tag{1b}$$

$$\dot{\phi}(t) = {}^1/_{\tau_\phi}(K_\phi \phi_d(t) - \phi(t)), \tag{1c}$$

$$\dot{\theta}(t) = {}^1/_{\tau_\theta}(K_\theta \theta_d(t) - \theta(t)), \tag{1d}$$

where $\boldsymbol{p} = [p_x, p_y, p_z]^\top \in \mathbb{R}^3$ is the position, $\boldsymbol{v} = [v_x, v_y, v_z]^\top \in \mathbb{R}^3$ is the vector of linear velocities, $\boldsymbol{f} = [f_x, f_y, f_z]^\top \in \mathbb{R}^3$ is the external forces align each axis of the MAV, $\phi \in \mathbb{R} \cap [-\pi, \pi]$ and $\theta \in \mathbb{R} \cap [-\pi, \pi]$ are the roll and pitch angles, and $\boldsymbol{R}_{x,y}$ is the rotation matrix about the x and y axes, $T \in \mathbb{R}^+$ is the mass-normalized thrust, g is the gravitational acceleration, A_x, A_y, and $A_z \in \mathbb{R}$ are the normalized mass drag coefficients. The low-level control system is approximated by first-order dynamics driven by the reference pitch and roll angles ϕ_d and θ_d with gains of $K_\phi, K_\theta \in \mathbb{R}^+$, and time constants of $\tau_\phi \in \mathbb{R}^+$, $\tau_\theta \in \mathbb{R}^+$.

4. Nonlinear model predictive control

The objective of the NMPC scheme is to track the reference trajectory $\boldsymbol{x}_r = [\boldsymbol{p}, \boldsymbol{v}, \phi, \theta]^\top$ from the operator or a mission planner, while considering the estimated external forces from the NMHE and generating thrust T and attitude commands ϕ_d, θ_d for the low-level controller. The NMPC is solved online by the utilization of PANOC (Sathya et al., 2018) in order to guarantee overall real-time performance.

The states of the non-linear dynamics of the MAV according to Eq. (1), can be presented as $\boldsymbol{x} = [p_x, p_y, p_z, v_x, v_y, v_z, \phi, \theta]^\top$, the estimated states $\hat{\boldsymbol{x}} = [\hat{p}_x, \hat{p}_y, \hat{p}_z, \hat{v}_x, \hat{v}_y, \hat{v}_z, \hat{\phi}, \hat{\theta}]^\top$, while $\boldsymbol{f} = [f_x, f_y, f_z]^\top$ are the estimated external forces from the NMHE. Finally, the control input is defined as $\boldsymbol{u} = [T, \phi_d, \theta_d]^\top$. Based on the Euler method for a sampling time T_s, the discrete-time dynamical system is obtained as $\boldsymbol{x}_{k+1} = f(\boldsymbol{x}_k, \boldsymbol{u}_k)$.

The NMPC solves at each instant k a finite horizon problem with a prediction horizon N. The states and the control actions in $k + j$ steps ahead of the current time step k are indicated as $\boldsymbol{x}_{k+j|k}$ and $\boldsymbol{u}_{k+j|k}$ correspondingly. At each time step, an optimal sequence of control actions $\boldsymbol{u}^\star_{k|k}, \ldots, \boldsymbol{u}^\star_{k+N-1|k}$ are obtained by the NMPC based on the reference and current state of the system, while the first control action $\boldsymbol{u}^\star_{k|k}$ is applied to the low-level controller by utilizing a zero-order hold element. Thus, at each instant, the $\boldsymbol{u}(t) = \boldsymbol{u}^\star_{k|k}$ for $t \in [kT_s, (k+1)T_s]$ is fed to the low-level controller. The following finite horizon cost function is introduced for the proposed NMPC:

$$J = \sum_{j=0}^{N-1} \underbrace{\|\boldsymbol{x}_{k+j+1|k} - \boldsymbol{x}_r\|^2_{Q_x}}_{\text{waypoint error}} + \underbrace{\|\boldsymbol{u}_{k+j+1|k} - \boldsymbol{u}_r\|^2_{Q_u}}_{\text{actuation}} + \underbrace{\|\boldsymbol{u}_{k+j|k} - \boldsymbol{u}_{k+j-1|k}\|^2_{Q_{\Delta u}}}_{\text{smoothness cost}}. \tag{2}$$

As defined on the first term of the objective function, the deviation of the current state $\boldsymbol{x}_k$ from the desired state $\boldsymbol{x}_r$ is penalized for the accurate tracking of the reference. The second term is the hovering term, where $\boldsymbol{u}_{ref}$ is $[g, 0, 0]^\top$, which is the hover thrust with horizontal angles. The last term of the objective function penalizes the aggressiveness of the obtained control actions. Additionally, $\boldsymbol{Q}_x \in \mathbb{R}^{8\times8}$, $\boldsymbol{Q}_u \in \mathbb{R}^{3\times3}$, $\boldsymbol{Q}_{\Delta u} \in \mathbb{R}^{3\times3}$ are the weights for each term of the objective function, which reflects their relative importance of them.

To limit the control actions of the NMPC within a range, the control input $\boldsymbol{u}$ is bounded as it follows:

$$0 \le T \le T_{max} \tag{3a}$$

$$\phi_{min} \le \phi_d \le \phi_{max} \tag{3b}$$

$$\theta_{min} \le \theta_d \le \theta_{max} \tag{3c}$$

The constraints are implemented to avoid aggressive behavior during maneuvers and represent the desired physical constraints of the platform. Based on the previous definitions, the following optimization problem is defined in (4).

$$\min_{\{u_{k+j|k}\}_{j=0}^{N-1}} J \tag{4a}$$

$$\text{s.t.} \quad \boldsymbol{x}_{k+j+1|k} = f(\boldsymbol{x}_{k+j|k}, \boldsymbol{u}_{k+j|k}), \tag{4b}$$

$$\text{Constraints (3a), (3b), (3c).} \tag{4c}$$

5. Nonlinear moving horizon estimation

The proposed NMHE (Rao, Rawlings, & Mayne, 2003) estimates the system's states and external forces applied to the MAV. Fig. 3 depicts the effect of the external forces on the body frame of the MAV. The body frame forces f_x, f_y, f_z result in the position drift of the MAV in the x, y, z body axes correspondingly.

For the NMHE formulation, the (1) is presented in the discrete time form as:

$$\bar{\boldsymbol{x}}_{k+1} = \mathcal{F}(\bar{\boldsymbol{x}}_k, \boldsymbol{u}_k) + \boldsymbol{w}_k, \tag{5a}$$

$$\boldsymbol{y}_k = \mathcal{H}(\bar{\boldsymbol{x}}_k) + \boldsymbol{\Lambda}_k, \tag{5b}$$

where, $\bar{\boldsymbol{x}} = [\boldsymbol{x}, \boldsymbol{f}]^\top$, $\mathcal{F} : \mathbb{R}^{n_s} \times \mathbb{R}^{n_u} \to \mathbb{R}^{n_s}$ is a nonlinear function, $\mathcal{H} : \mathbb{R}^{n_s} \to \mathbb{R}^{n_m}$ is a linear vector function of the states $\bar{\boldsymbol{x}}$, and $\boldsymbol{y} = [x, y, z, v_x, v_y, v_z, \phi, \theta]^\top$ is the measured output. Furthermore, n_s, n_u, and n_m are the number of states, inputs and measurements, respectively, $\boldsymbol{\Lambda}_k \in \mathbb{R}^{n_m}$ and $\boldsymbol{w}_k \in \mathbb{R}^{n_s}$ represent the measurement noise and the model disturbances correspondingly. It should be highlighted that in the NMHE formulation the external forces are considered in the state space of the dynamic model, thus in the NMHE formulation, $\boldsymbol{f}$ is considered as an unmeasured state, while in the NMPC formulation, $\boldsymbol{f}$ is variable for the prediction horizon, which is updated based on the NMHE estimations. The external force $\boldsymbol{f}$ changes over the time, however in each estimation window it is assumed that the external force is static ($\dot{\boldsymbol{f}} = 0$).

The process disturbance $\boldsymbol{w}_k$, the measurement noise $\boldsymbol{\Lambda}_k$, and the initial Probability Density Function (PDF) of the state vector are unknown and it is assumed that they are randomly distributed according to the Gaussian PDF with covariance matrices $\boldsymbol{Q} \in \mathbb{R}^{n_s \times n_s}$, $\boldsymbol{\Omega} \in \mathbb{R}^{n_m \times n_m}$, and $\boldsymbol{\Psi} \in \mathbb{R}^{n_s \times n_s}$, respectively (Ungarala, 2009). Furthermore, the initial condition $\tilde{x}_0$ is assumed to be known. In a stochastic state estimation, such as NMHE, it is assumed that the probability distribution of the measurement noise $\boldsymbol{\Lambda}$ and the state disturbance $\boldsymbol{w}_k$ are known. Based on that information, the estimated states are obtained by calculating the maximum of PDF (Rao & Rawlings, 2000). Furthermore, it is assumed that the measurement noise and the state disturbances have normal (or Gaussian) distribution. The Gaussian distribution is the most common distribution for the noise since only the mean value and the standard deviation of the noise are required. Additionally, according to the central limit theorem, the sum of infinity large Independent Identically Distributed (IID) random variables will converge to the Gaussian (normal) distribution (Rojas, 2010). It should be noted that in the case of a nonlinear system model, the distribution of variables will not always stay Gaussian (López-Negrete, Patwardhan, & Biegler, 2011). Therefore, updating the covariance matrix can lead to a better distribution of data at each iteration, thus as future work, an EKF or a particle filter could be utilized for updating the covariance matrix.

Based on the information about random noises and a set of available noisy measurements $\boldsymbol{Y} = \{\boldsymbol{y}_j : j = 1, \dots, N_e\}$, the estimated states of the system $\bar{\boldsymbol{X}} = \{\bar{\boldsymbol{x}}_j : j = 0, \dots, N_e\}$ are obtained by solving the following optimization problem in (6), while the N_e is the length of the fixed horizon window. Moreover, $\bar{\boldsymbol{x}}_{k-j|k}$ and $\boldsymbol{y}_{k-j|k}$ are the $k-j$ previous state and measurements form the current time k.

$$\min_{\bar{\boldsymbol{x}}_{(k-N_e|k)}, \boldsymbol{W}^{(k-1|k)}_{(k-N_e|k)}} J(k) \tag{6a}$$

$$\text{s.t. } \bar{\boldsymbol{x}}_{i+1|k} = \mathcal{F}(\bar{\boldsymbol{x}}_{i|k}, \boldsymbol{u}_{i|k}) + \boldsymbol{w}_{i|k} \tag{6b}$$

$$\boldsymbol{y}_{i|k} = \mathcal{H}(\bar{\boldsymbol{x}}_{i|k}) + \boldsymbol{\Lambda}_{\mathbf{i|k}} \quad i = \{k - N_e, \dots k - 1\} \tag{6c}$$

$$\boldsymbol{w}_k \in \mathbb{W}_k, \quad \boldsymbol{\Lambda}_k \in \mathbb{\Lambda}_k, \quad \bar{\boldsymbol{x}}_k \in \mathbb{X}_k \tag{6d}$$

where,

$$\begin{aligned} J(k) = & \underbrace{\|\bar{\boldsymbol{x}}_{k-N_e|k} - \tilde{\boldsymbol{x}}_{k-N_e|k}\|^2_{\boldsymbol{\Psi}}}_{\text{arrival cost}} + \sum_{i=k-N_e}^{i=k} \underbrace{\|\boldsymbol{y}_{i|k} - \mathcal{H}(\bar{\boldsymbol{x}}_{i|k})\|^2_{\boldsymbol{\Omega}}}_{\text{stage cost}} \\ & + \sum_{i=k-N_e}^{i=k-1} \underbrace{\|\bar{\boldsymbol{x}}_{i+1|k} - f(\bar{\boldsymbol{x}}_{i|k}, \boldsymbol{u}_{i|k})\|^2_{\boldsymbol{Q}}}_{\text{stage cost}} \end{aligned} \tag{7}$$

In (6) $\boldsymbol{W}^{(k-1|k)}_{(k-N_e|k)} = col(\boldsymbol{w}_{(k-N_e|k)}, \dots, \boldsymbol{w}_{(k-1|k)})$ is the estimated process disturbance from time $k - N_e$ up to $k - 1$, which is estimated at the time k and the estimation horizon is defined with a fixed window of size $N_e \in \mathbb{Z}^+$.

The first term of the objective function in (7) is the arrival cost weighted by $\boldsymbol{\Psi}$, which describes the uncertainty in the initial state at the beginning of the horizon considering the error between the observation model and the predicted initial state $\tilde{\boldsymbol{x}}(k - N_e \mid k)$. In general, there are different approaches to transfer the arrival cost at each time (Ungarala, 2009), while in this work, the smoothing approach is used that only uses one time-step before the window to approximate the arrival cost. The second and third terms are called stage costs. The $\|\boldsymbol{y}_{i|k} - \mathcal{H}(\bar{\boldsymbol{x}}_{i|k})\|^2$, weighted by $\boldsymbol{\Omega}$, is the bias between the measured output and the estimated state. The $\|\bar{\boldsymbol{x}}_{i+1|k} - f(\bar{\boldsymbol{x}}_{i|k}, \boldsymbol{u}_{i|k})\|$, weighted by $\boldsymbol{Q}$, is the estimated model disturbance.

At every instant k, a finite-horizon optimal problem with horizon window of N_e is solved and the corresponding estimated states and external forces sequence of $\bar{\boldsymbol{x}}^\star_{k-N_e|k}, \dots \bar{\boldsymbol{x}}^\star_{k-1|k}$ are obtained. The final estimated state $\bar{\boldsymbol{x}}^\star_{k-1|k}$ is fed to the controller.

5.1. Embedded optimization

The proposed NMPC (4) and NMHE (6) frameworks, can be solved with PANOC with single shooting formulation (Sathya et al., 2018). The gradient of the objective functions is obtained from the automatic differentiation (Dunn & Bertsekas, 1989) in CasADi (Andersson, Gillis, Horn, Rawlings, & Diehl, 2019). The Optimization Engine (OpEn) is a real-time embedded nonconvex optimization that combines the PANOC with the penalty method to compute approximate stationary points of nonconvex problems, while the study in Sopasakis et al. (2020) provides an extensive overview and comparison of the OpEn with other optimization methods such as Interior Point OPTimizer (IPOPT), Sequential Least Squares Programming (SLSQP).

PANOC provides high accuracy and fast convergence solutions due to their numerical properties. However, PANOC cannot guarantee a global solution to the problem. As a future work, meta-heuristic optimization algorithm (Yang, 2011) such as particle swarm optimization (Abualigah et al., 2019; Kennedy, Kennedy, Eberhart, & Shi, 2001) or genetic algorithm (Davis, 1991) can be considered for global optimal solutions. These algorithms usually lead to “good enough” solutions, within a reasonable amount of time. Therefore, they have attracted a lot of attention with new algorithms proposed recently with improvement in performance every day (Abualigah et al., 2021). It should be highlighted that in most of the cases, the computation time limits the use of such algorithms for the fast dynamics of aerial robots.

6. Results

The proposed framework for estimating and compensating external forces described in Sections 4 and 5 is evaluated under simulation and experimentation scenarios. Initially, in order to prove the performance but also to compare the methodology with similar methods, while the external forces are known, a MAV model is evaluated in a simulation environment for different estimators. Furthermore, to evaluate the use and the application range of the proposed framework, a series of various experimental trials are presented where the external forces are generated by different means.

6.1. Simulation evaluation

Initially, the proposed method is evaluated in a computer based simulation with an Intel Core i7-6600U CPU, 2.6 GHz and 8 GB RAM. The main purpose is to evaluate the proposed architecture with noisy measurements and known external forces. In this case, the MAV model parameters, as defined in (1), are presented in the Table 2.

The NMPC and NMHE parameters are indicated in Tables 3 and 4, respectively. The prediction horizon N_p for the NMPC and the estimation window N_e for the NMHE is 40. It should be highlighted that in case of the NMPC the control inputs are the decision variables, while in case of the NMHE the states and external forces $\bar{\boldsymbol{x}}$ are the decision variables.

The generated noise follows a normal Gaussian distribution $\mathcal{N}(\mu, \sigma^2)$ (Peebles, 2001), while μ and σ^2 are the mean and variance, respectively. The noise is generated separately for each term of the states, while the position estimations suffer from higher uncertainties compared to velocity estimations (Siegwart, Nourbakhsh, & Scaramuzza, 2011), since position drift is more difficult to recover when compared to the velocity drift that can be recovered after a few time steps. The normal Gaussian distribution, for the position is $\mathcal{N}(0, 1\,\text{m})$ and for the velocity estimation is $\mathcal{N}(0, 0.5\,\text{m/s})$. In the following simulation results, the MAV takes off from the ground and the $\boldsymbol{x}_r$ is set to $[0, 0, 5, 0, 0, 0, 0, 0]^\top$. The random external forces are generated every 20 s and they are kept active for that interval until a new random external force is generated, while the overall simulation time is 240 s.

Fig. 4 shows the measured, estimated, and actual values of the MAV position in the presence of external disturbances. The NMHE tracks the actual value and reduces the noise in measurements, while

Table 2
Selected tuning parameters of the MAV model during simulations.

g	A_x	A_y	A_z	K_ϕ	K_θ	τ_ϕ	τ_θ
$9.8\,\text{m/s}^2$	0.1	0.1	0.2	1	1	0.5 s	0.5 s

Table 3
NMPC simulation weight parameters and constraints.

$\boldsymbol{Q}_x$	$\boldsymbol{Q}_u$	$\boldsymbol{Q}_{\Delta u}$
$[10, 10, 10, 5, 5, 5, 1, 1]^\top$	$[10, 10, 10]^\top$	$[20, 20, 20]^\top$
T	ϕ	θ
$[0, 1] \cap \mathbb{R}$	$[-0.4, 0.4] \cap \mathbb{R}$ rad	$[-0.4, 0.4] \cap \mathbb{R}$ rad

Table 4
NMHE simulation tuning parameters.

$\boldsymbol{\Psi}$	$\boldsymbol{Q}$	$\boldsymbol{\Omega}$
$\mathbf{I}_{11}$	$\mathbf{I}_8$	$5 \times \mathbf{I}_{11}$

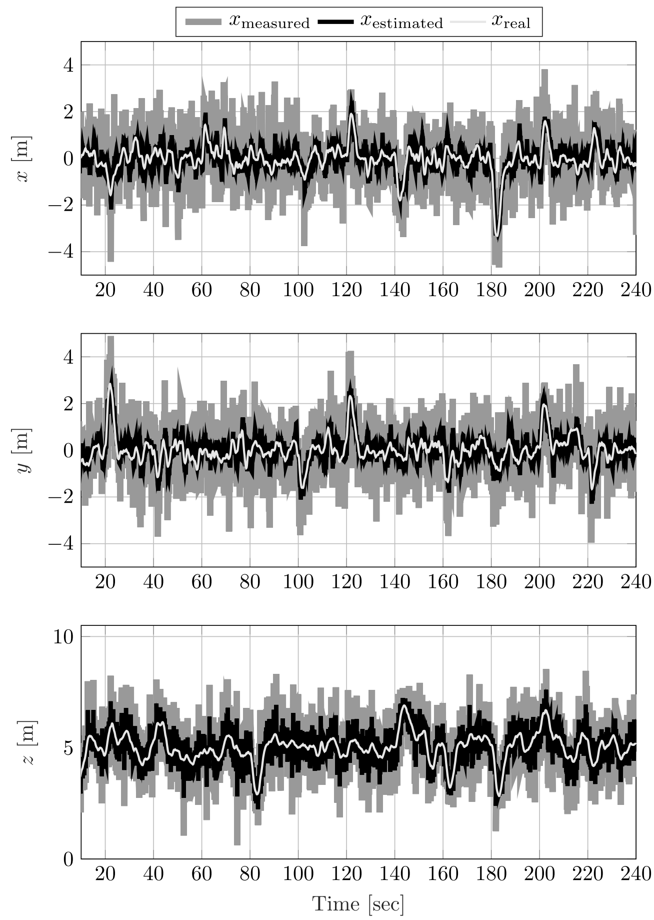

Fig. 4. Simulated position $[x, y, z]^{\top}$ in meters, where the measured, real and estimated values are shown by gray, white and black colors, respectively.

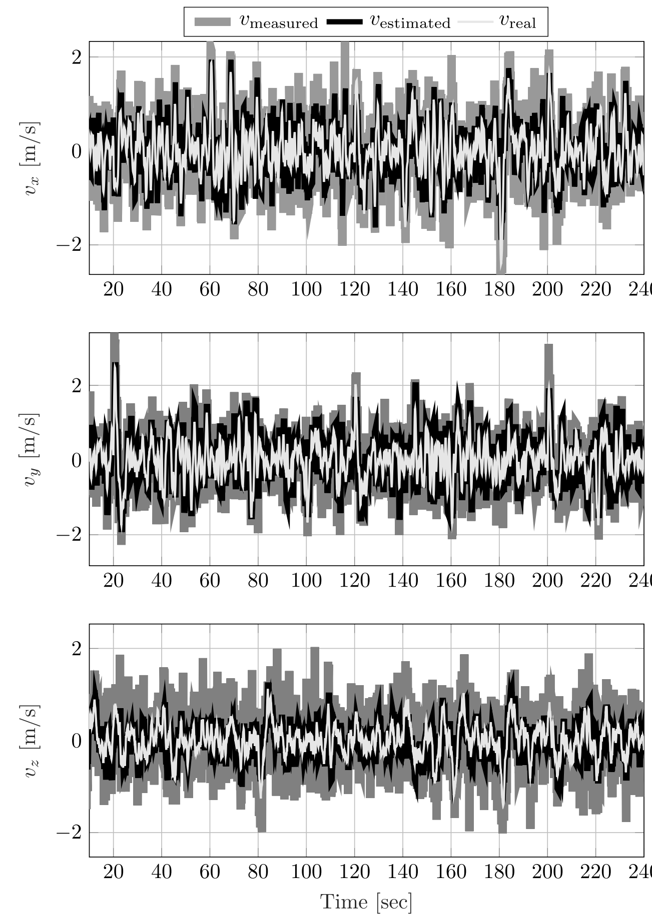

Fig. 5. Simulated velocity states $[v_x, v_y, v_z]^{\top}$ in m/s, where the measured, real and estimated values are shown by gray, white and black colors, respectively.

the Root Mean Square Error (RMSE) of the estimation is $0.3\,\text{m}$ for x, y, z positions. It should be noted that the RMSE between the noisy measurements and the actual values is $1\,\text{m}$.

Fig. 5 depicts the body frame measured, estimated and actual velocities. A significant improvement of the estimated velocities compared to the measured ones can be noticed. The RMSE of the estimated velocity from the true velocity is $0.3\,\text{m/s}$.

Table 5
Performance comparison between the proposed NMHE framework and other state-of-art methods.

	EKF	UKF	NMHE
Est. external forces RMSE [N]	1.04	0.78	0.62
Reference tracking RMSE [m]	1.88	1.44	0.72
Average comp. time [ms]	8.9	22.3	5.4
Average convergence [s]	3.24	7.25	2.99

Table 6
NMPC tuning parameters and constraints for the experimental evaluation with the fan.

$\boldsymbol{Q}_x$	$\boldsymbol{Q}_u$	$\boldsymbol{Q}_{\Delta u}$
$[10, 10, 10, 5, 5, 5, 1, 1]^{\top}$	$[10, 10, 10]^{\top}$	$[20, 20, 20]^{\top}$
T	ϕ	θ
$[0, 1] \cap \mathbb{R}$	$[-0.8, 0.8] \cap \mathbb{R}$ rad	$[-0.8, 0.8] \cap \mathbb{R}$ rad

Table 7
NMHE tuning parameters for the experimental evaluation with the fan.

$\boldsymbol{\Psi}$	$\boldsymbol{Q}$	$\boldsymbol{\Omega}$
$\mathbf{I}_{11}$	$\mathbf{I}_{8}$	$\mathbf{I}_{11}$

Table 8
NMPC tuning parameters and constraints for the experimental evaluation with the wind-wall.

$\boldsymbol{Q}_x$	$\boldsymbol{Q}_u$	$\boldsymbol{Q}_{\Delta u}$
$[5, 5, 5, 5, 5, 5, 1, 1]^{\top}$	$[10, 10, 10]^{\top}$	$[20, 20, 20]^{\top}$
T	ϕ	θ
$[0, 1] \cap \mathbb{R}$	$[-0.6, 0.6] \cap \mathbb{R}$ rad	$[-0.6, 0.6] \cap \mathbb{R}$ rad

The proposed NMHE-NMPC framework is compared with an EKF-based and UKF-based framework. The noises and external forces are identical for the best comparison among all tests. In addition, for every simulation, the same NMPC module is used to regulate the position of the MAV based on the estimated external disturbances.

The introduced external forces vary following a step response at $20\,\text{s}$ intervals instead of being updated gradually, which would ease the estimation convergence. It should be highlighted that the external forces are unmeasured states for the estimators, and they provide estimates without knowledge of the actual external forces value. All three

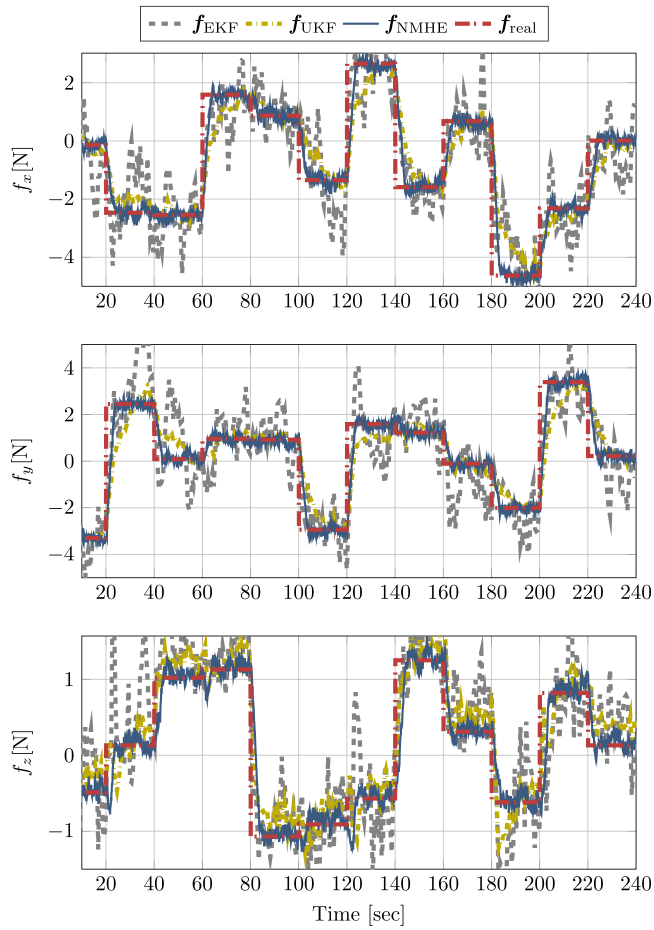

Fig. 6. Generated external forces $[f_x, f_y, f_z]^\top$ in comparison to the estimated external forces from the NMHE, the EKF and the UKF of the simulation scenario.

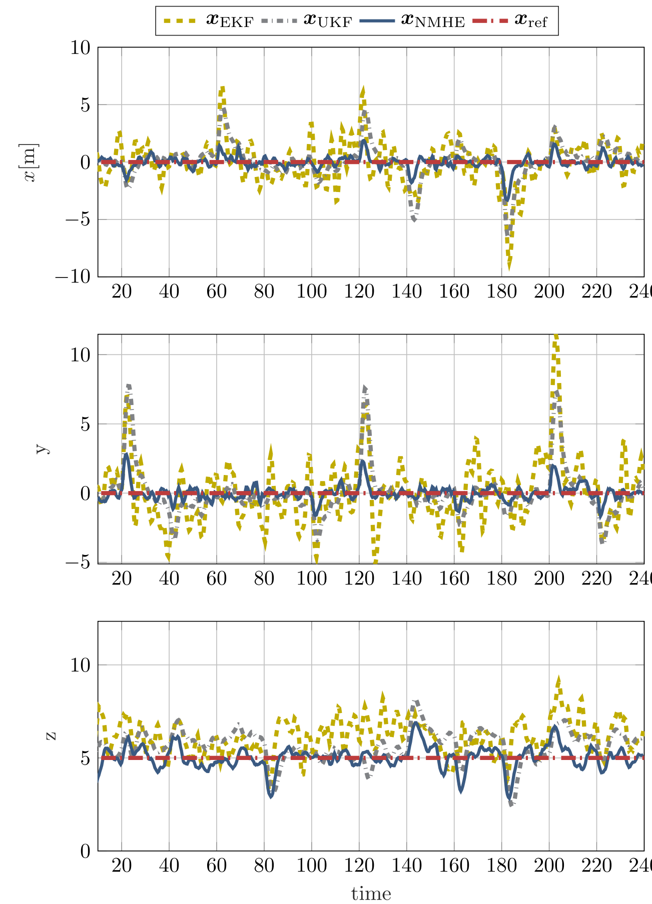

Fig. 7. Simulated MAV position compared to the reference point based on EKF, UKF, and NMHE external force rejection frameworks, respectively.

methods have been tuned based on the noise properties to enhance their estimation capabilities.

The external force estimation comparison among EKF, UKF and the proposed NMHE method is depicted in Fig. 6. As it can be observed the convergence time of the EKF and the NMHE is almost the same, but in contrast, the EKF appears to be less accurate on the estimation performance. On the other hand, the UKF appears to have accurately estimate the forces, but the convergence is quite slow compared to NMHE.

Fig. 7 presents the positions x, y, and z of the MAV based on the EKF, the UKF, and the NMHE methods. As a result of the external force estimation performance (Fig. 6), the EKF-NMPC framework appears to have the worst tracking behavior with a max error from the reference point 6.7, 11.4, and 4.1 m for the x, y, and z axes, respectively. The UKF-NMPC has slightly better performance, and the maximum drifts reference points 4.4, 7.7, and 3.2 m for the x, y, and z axes, respectively. Lastly, the proposed framework presents the minimum drift from the reference point 3.3, 2.8, and 2.2 m meters for the x, y, and z axes, respectively.

Table 5 shows a comparison between the proposed NMHE-NMPC versus EKF-NMPC and UKF-NMPC frameworks. The NMHE presents the lowest overall RMSE for the estimated external forces, 0.62 N, while the UKF results to an RMSE value of 0.78 N. On the other hand, the highest overall RMSE appears for the EKF, 1.04 N. Similar results are observed for the position RMSE values with 1.88 m 1.44 m and 0.72 m for EKF, UKF, and NMHE, respectively. The average computation time of the UKF is higher from the NMHE and the UKF by 16.9 ms and 13.4 ms, respectively. Lastly, the EKF has a similar average convergence time with the NMHE in contrast to the UKF that is slower, approximately by 4 s.

Recapping the evaluation of the proposed framework in a simulation environment, the NMHE accurately tracks the states and successfully estimates the generated forces. Note that any variation in the position occurs due to the external forces, while the NMPC compensates them by considering the estimated external force values. Increasing the control action boundaries of the NMPC will result in better position tracking in the presence of external forces. The mean and max computation time of the NMHE is 5.4 ms and 8.5 ms, respectively. Moreover, the mean and max solver time of the NMPC is 1.9 ms and 5.9 ms, respectively. The lower computation time of the NMPC is primarily due to the smaller number of decision variables compared to the NMHE. The NMPC has $n_u \times N_p$ decision variables, and NMHE has $n_s \times N_p$, 120, and 440 decision variables, respectively.

6.2. Experimental evaluation

A quadcopter (Fig. 8(a)), based on the ROSflight flight controller, is used to evaluate the proposed method. The Aaeon UP-Board is the

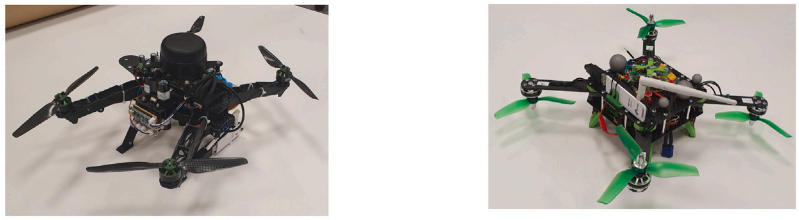

(a) Standard MAV (b) Re-configurable MAV

Fig. 8. Experimental quadcopter platforms used for the evaluation of the proposed methodology.

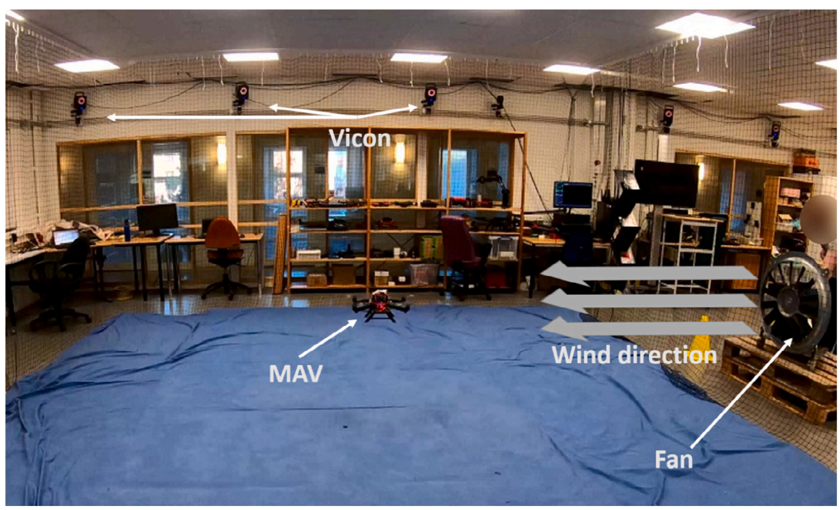

Fig. 9. Photographic still of the flying arena at LTU. The fan is located in the right side while the flying MAV is located in the center of the arena.

main processing unit, incorporating an Intel Atom x5-Z8350 processor and 4 GB RAM. The operating system running on-board is the Ubuntu Desktop 18.04, while Robot Operating System (ROS) Melodic is utilized. The four different scenarios defined in the sequel to evaluate the proposed method utilize the same platform. The second platform used for evaluation is a re-configurable quadcopter (Fig. 8(b)). The second platform is equipped with the same computation board and operating system. Both aerial robots are designed and built by the Robotics & AI Team at LTU (Kominiak, Mansouri, Kanellakis, & Nikolakopoulos, 2020).

The MAV dynamics presented in (1) are based on Euler angles, and although this formulation is easy to implement, it suffers from the presence of singularities ("gimbal lock" problem), thus cannot define certain orientations (Fresk & Nikolakopoulos, 2013). Moreover, the flying arena has limited dimensions in both experimentation locations (LTU and CAST). The control inputs are bounded based on the experiment to avoid gimbal lock and consider safety criteria. Thus, the limit is increased to the maximum possible value to avoid high wind gusts while considering the arena dimensions and singularity issues.

In all the experimental evaluations the NMPC and NMHE sampling time is $0.02\,\mathrm{s}$ and the solver uses only 10% of the CPU usage on the Aaeon UP-Board. Link: https://youtu.be/u6gQuL-oqWY provides a video summary of the overall experiments.

6.2.1. Evaluation with wind tunnel fan

In this first case, the method is evaluated when a fan generates the wind gusts, while an operator control the fan speed manually. Fig. 9 depicts the flying area, the dimension of the arena is $4 \times 4 \times 3$ m^3. In all the cases, the $\boldsymbol{x}_\mathrm{r}$ for the NMPC is set to $[0, 0, 0.6, 0, 0, 0, 0, 0]^\top$, while the fan is located in the right side of the platform, which generates mainly wind in y-axis of the MAV body frame. The Vicon Motion-capture system is used for precise quadcopter localization in this experiment. The NMPC and NMHE parameters in this case are presented in the Tables 6 and 7, respectively.

Fig. 10 depicts the estimated and the measured values of the position of the MAV from the NMHE and the Mo-Cap system Vicon, respectively. An operator increases the fan speed; however, there was

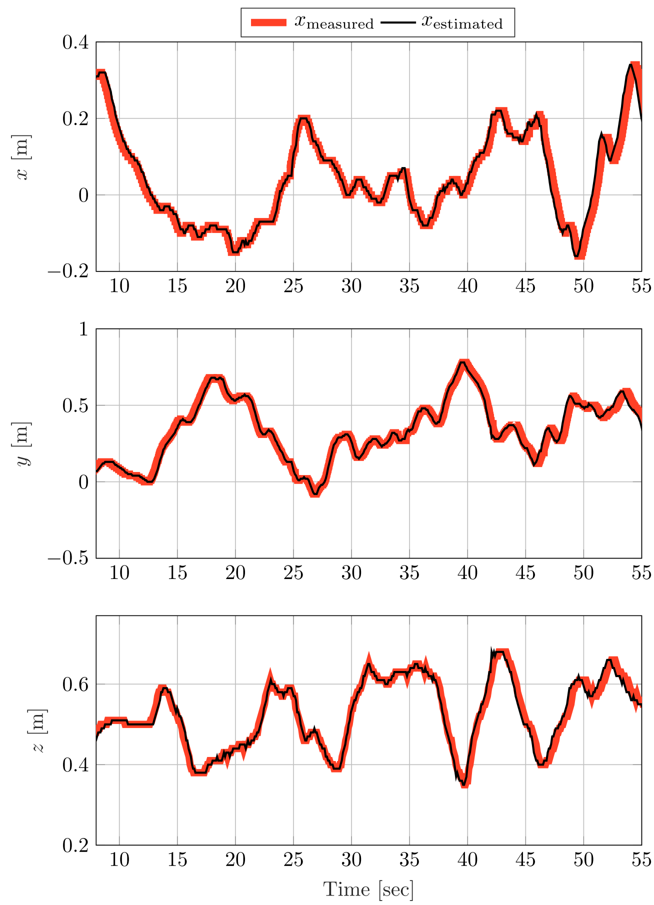

Fig. 10. Position states $[x, y, z]^{\top}$ of the experimental scenario where the wind is generated from a fan. The measured and estimated values are shown by gray and black colors, respectively.

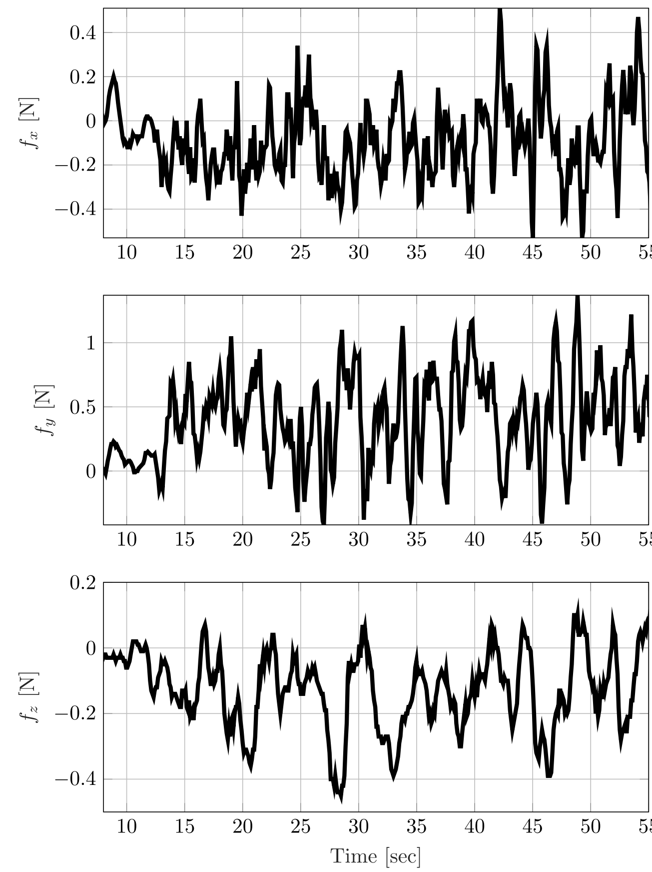

Fig. 11. Estimated forces $[f_x, f_y, f_z]^{\top}$, of the experimental scenario where the wind is generated from a fan.

no hardware to measure the actual power consumption of the fan. Based on Air Velocity Anemometer, the wind speed in the arena reaches 7.5 m/s. The RMSE between the real and estimated measurements is 0.1 m, while it is worth mentioning that the measurement noise is low and can be considered negligible.

Fig. 11 depicts the estimated external force for this scenario. It can be seen that the f_y has higher values in comparison to the forces in the other axes. This is due to the location of the fan which mainly generates wind in the y-axis body frame of the MAV. The mean and absolute max value of the forces in x, y, and z axis are $(-0.12, 0.52)$ N, $(0.3, 1.4)$ N, and $(-0.28, 0.48)$ N, respectively. The RMSE between the $\boldsymbol{x}$ and $\boldsymbol{x}_r$ is 0.2 m, 0.5 m, and 0.3 m for x, y, and z for axes, respectively.

Fig. 12 depicts the position of the MAV, when the NMHE module is not used and the NMPC does not have any information of the estimated external forces. In this case, the $\boldsymbol{x}_r$ and the NMPC parameters are same as in the previous experiment with the fan. The RMSE between position and reference point for x, y and z axes is 0.5 m, 0.5 m, and 0.56 m, respectively, while the maximum absolute error observed to be 1.5 m in the body frame y-axis. It should be highlighted that due to the large error in the y-axis and the limited size of the area the maximum wind speed for this case reaches to 1.5 m/s, which is 6 m/s less than the case with the NMHE module.

6.2.2. Evaluation with wind generated with wind-wall

In this case, the proposed modules are evaluated in CAST laboratory at the California Institute of Technology. Fig. 13 depicts the flying arena, where the wind-wall is located on the left side and generates wind towards x-axis of the MAV (due to the reference heading of the platform). The wind-wall dimension is 2 m and 2.1 m for the width and height, with total number of 18 fan modules. The modules can produce a maximum wind speed of 16 m/s.

In this case, the Mo-Cap system *OptiTrack* is used for providing localization information. Table 8 provides the parameters for the NMPC and the NMHE is same as experiment with the fan in Table 7.

Fig. 14 depicts the estimated and measured position of the MAV, while the RMSE between the measured and estimated values is 0.1 m. The waypoint $\boldsymbol{x}_r$ is set to $[0.5, -1.6, 2.0, 0, 0, 0, 0, 0]^{\top}$, and the RMSE between the $\boldsymbol{x}$ and $\boldsymbol{x}_r$ is 0.2 m, 0.18 m, and 0.25 m for x, y, and z axes, respectively.

The estimated external forces of the wind-wall are depicted in Fig. 15. The mean and absolute max value of the forces for each axis x, y, and z are $(-1.2, 2.2)$ N, $(-0.2, 0.9)$ N, and $(0.2, 0.55)$ N, respectively.

Fig. 16 shows the power percentage of the wind-wall in the proposed experiment. The operator increases the power of the wind-wall from zero to 55%, which generates an airflow of up to 8.8 m/s. As the wind-wall faces towards the MAV x-axis, the estimated force f_x is gradually decreasing by following the same trend of the increasing wind-wall power percentage.

Moreover, the MAV is evaluated with the use of the NMPC module and without the NMHE module, thus the external forces are not estimated. In this case, the $\boldsymbol{x}_r$ is set to $[0.5, -1.6, 1.3, 0, 0, 0, 0, 0]^{\top}$ and the same tuning of the NMPC is used. Fig. 17 depicts the position of the MAV. The RMSE of the position and the waypoint for x, y and

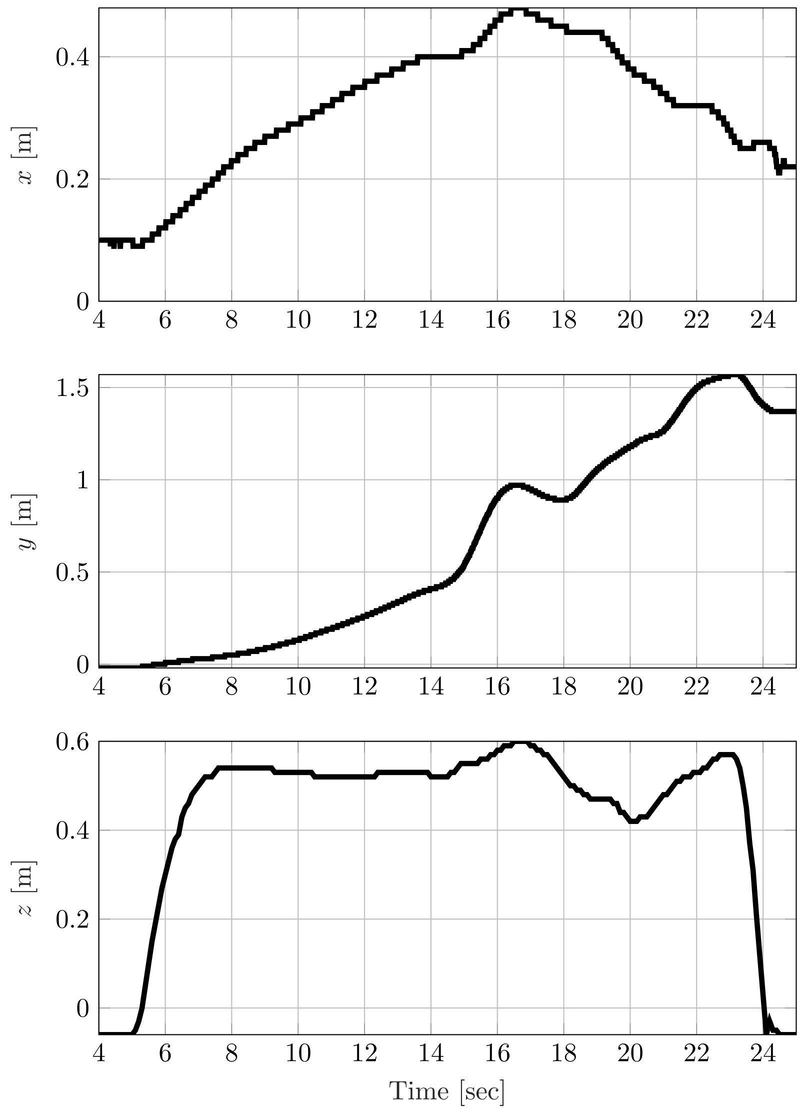

Fig. 12. MAV position, while the NMHE module is disabled and the NMPC has no information of the external forces for the experimental scenario where the wind is generated from a fan.

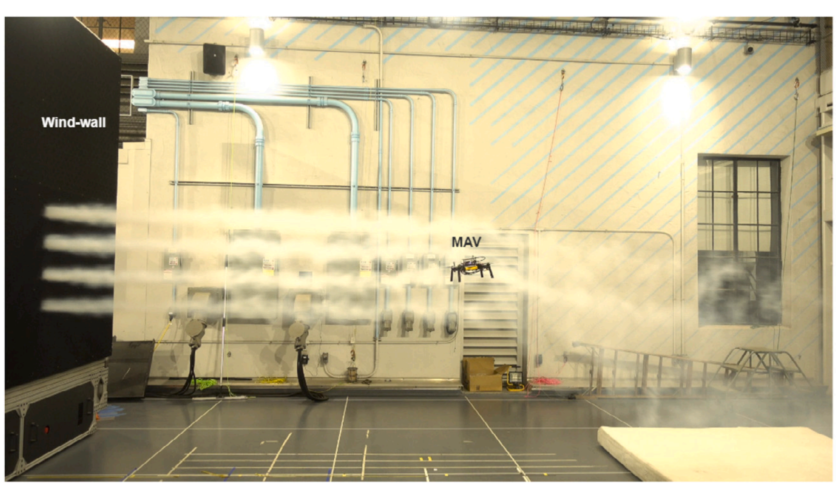

Fig. 13. Flying arena in CAST laboratory at the California Institute of Technology. In the left side of the illustration is the wind-wall and in the middle is the flying MAV.

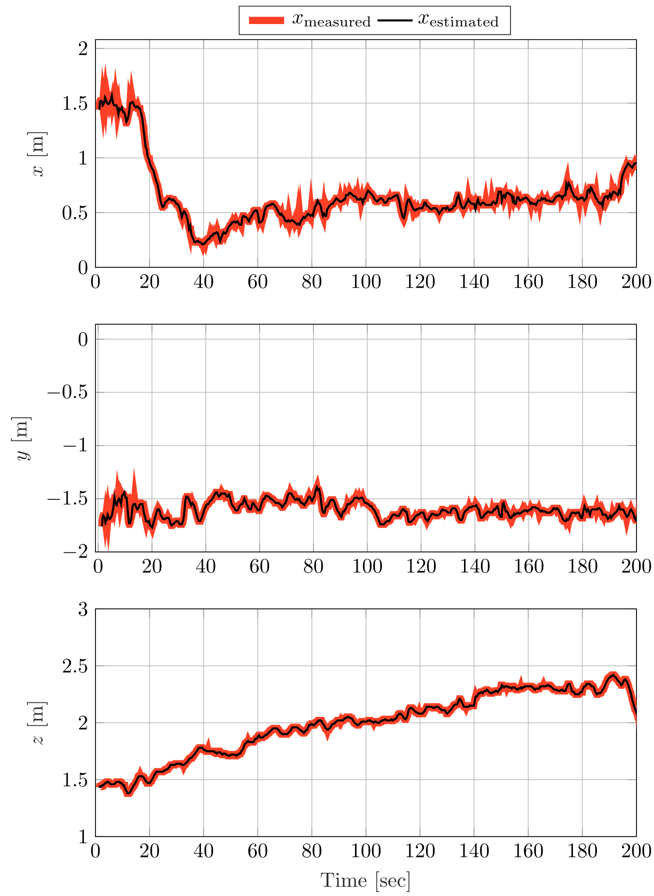

Fig. 14. Position states $[x, y, z]^{\top}$ of the scenario where the wind is generated from a wind-wall. The measured and estimated values are shown by gray and black colors, respectively.

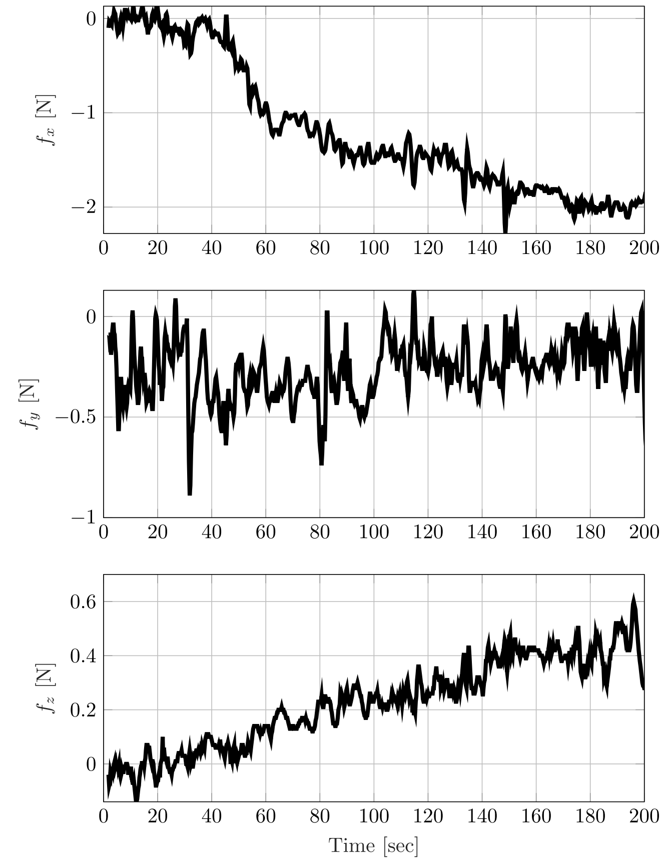

Fig. 15. External force estimates $[f_x, f_y, f_z]^{\top}$, for the scenario where the wind is generated from a wind-wall.

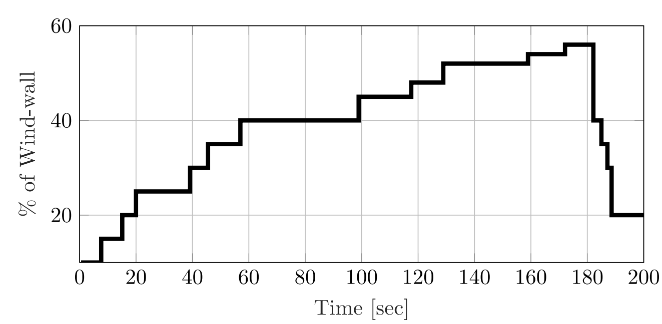

Fig. 16. Wind-wall power percentage for the case of the MAV subject to winds estimated up to 8.8 m/s.

z axes is 0.46 m, 0.35 m, and 0.40 m respectively, while the maximum absolute error in x-axis is 1.58 m. This is due to the generated wind towards the x-axis of the MAV. Moreover, Fig. 18 shows the power percentage of the wind-wall which approximately reaches up to 3.5 m/s. From the obtained results, it is observed that the NMPC tracks the desired waypoint with a high error when the external forces are not estimated. In addition, for this scenario, the maximum wind speed is approximately 2.5 times lower when compared to the previous case.

6.3. External force estimation with tethered payload

In this scenario, an external payload of 0.25 kg is tethered to the MAV, as depicted in Fig. 19. The tether length is 0.68 m, resulting in a period of motion of 1.65 s. To ensure the stability of the MAV-pendulum system, the NMHE and the NMPC modules frequency should be at least be twice the maximum frequency of the system (Marks, 1991). Thus, if the pendulum's motion increases in speed and amplitude, the system will eventually fall to instability. The scope of the proposed method is to reduce the effect of the swinging load, while an alternative method would be to augment the states of the system with the pendulum equations of motion to dampen the swinging of the pendulum (Kuře, Bušek, Vyhlídal, & Niculescu, 2019). The same parameters as in Tables 7 and 8 are used for this experimental scenario.

In this case, the $\boldsymbol{x}_r$ is set to $[-0.7, -1.6, 1.5, 0, 0, 0, 0, 0]^{\top}$ and $[0.0, -1.6, 1.5, 0, 0, 0, 0, 0]^{\top}$, which results MAV's hovering back and forth between the two setpoints and aligned with its x-axis. Fig. 20 depicts the position and estimated position of the MAV. The RMSE between the position and waypoint is 0.5 m, 0.4 m, and 0.2 m for x, y and z-axes, respectively.

Fig. 21 presents the estimated forces on the tether experiment. The oscillatory motion of the pendulum is evident in the estimated forces along the x and y axes of the platform. Note that when the MAV is approaching the landing set-point, a positive value for f_z is estimated. That occurs as the tether payload touches the ground and the force is omitted from the MAV. Worth highlighting that the standalone NMHE is not able to stabilize the aerial platform, and there is a

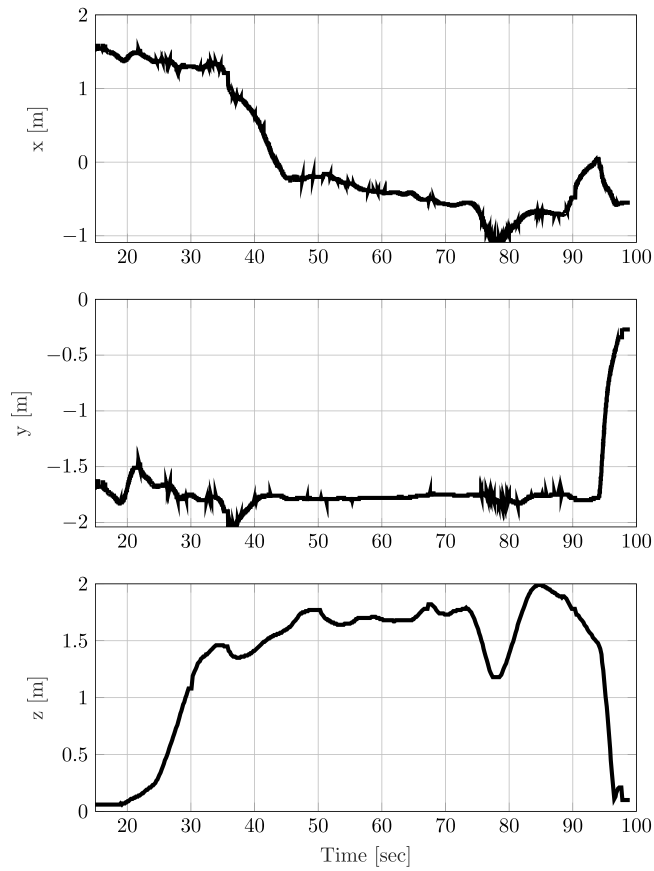

Fig. 17. Measured x, y, z positions of the MAV, without external forces estimation and compensation for the scenario where the wind is generated from a wind-wall.

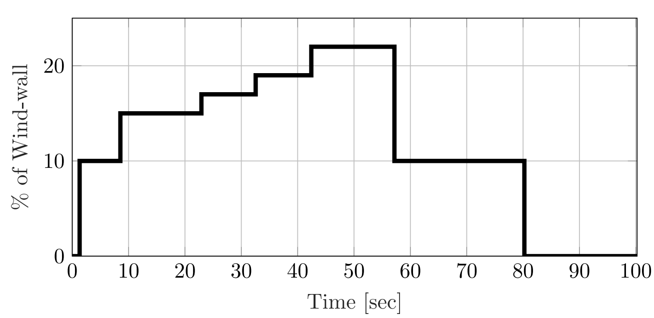

Fig. 18. Wind-wall power percentage for the case of the MAV subject to winds estimated up to 3.5 m/s.

need for compensation on the low-level controller; however, the NMHE estimation still provides collision-free navigation.

6.3.1. Evaluation with the MAV with re-configurable arms

This experiment involves a MAV with re-configurable arms to evaluate the performance of the external force estimation and the overall disturbance rejection proposed method. The MAV alters its configuration among H, X, Y, and T shapes based on the orientation of the arms as depicted in Fig. 22. The different MAV configurations have a direct impact on the moment of inertia of the platform and for asymmetric configurations, like Y and T, on its center of gravity (Falanga, Kleber, Mintchev, Floreano, & Scaramuzza, 2019).

Table 9
NMPC tuning parameters for the evaluation with the re-configurable MAV.

$\boldsymbol{Q}_x$	$\boldsymbol{Q}_u$	$\boldsymbol{Q}_{\Delta u}$
$[5,5,5,5,5,5,1,1]^{\top}$	$[10,10,10]^{\top}$	$[20,20,20]^{\top}$
T	ϕ	θ
$[0,1]\cap\mathbb{R}$	$[-1.0,1.0]\cap\mathbb{R}$ rad	$[-1.0,1.0]\cap\mathbb{R}$ rad

These dynamic variations drastically change the platform's balance, which under normal conditions would require a model-based control to be captured to avoid the collision of the platform. In contrast to the expectations, the same low-level control strategy, as in Section 2, has been utilized in the case of the re-configurable quadrotor. Thus, the low-level controller has zero adaptation to the morphology alterations. The selected methodology emphasizes the NMHE force estimation capabilities and disturbance rejection when significant changes occur in the platform dynamics. For the experimental evaluation the MAV is commanded to hold position at $\boldsymbol{x}_r = [0,0,0.6,0,0,0,0]^{\top}$ and the parameters of the NMPC in this case are presented in Table 9.

Fig. 23 depicts the position of the MAV and the estimated values. The initial RMSE, while the platform maintains the H and X formations for the first 35 s, stays at 0.11 m, 0.13 m, and 0.23 m for x, y, and z-axes, respectively. The higher altitude fluctuations occurred due to the aerodynamic effects and loss of energy among the propellers since there is overlap between them in H-formation. When the platform alters to the Y-formation and later on to the T-formation, the RMSE between the position and the waypoint is 0.7 m, 0.45 m, and 0.6 m for $x-y-z$ axes. The increased RMSE is expected as the asymmetry nature of those two formations result in a major shift of the platform's center of gravity.

Figs. 24 and 25 present the estimated forces of the NMHE and the generated control commands of the NMPC. The mean and absolute force levels are $(-0.18, 1.53)$ N, $(-0.14, 0.48)$ N, and $(0.06, 0.51)$ N for each axis x, y, and z. In Fig. 25 it is observed that the re-configurable drone reaches the input constraints, which are already expanded compared to the other experimental scenarios. More specifically, when the MAV changes to the T configuration, the input θ_d reaches closer to 1 rad, which is the NMPC bound for the pitch angle. It should be highlighted that the same experiment is performed without the NMHE module, and the stand-alone NMPC could not compensate for the arm re-configuration; thus, the experiment results in the collision of the platform with the protection net. As already emphasized, there is no model-based compensation for the low-level controller of the re-configurable MAV. Thus the high RMSE values are expected, while the MAV avoids the collision in contrast to the scenario where the NMHE module is suspended.

7. Concluding remarks

This article presented a novel embedded NMHE and NMPC modules for the external force estimation and disturbance rejection of a MAV. The proposed framework was evaluated and compared with state-of-the-art methods in simulation under varying force levels while the states of the system were affected by white noise. The experimental evaluation included four different scenarios of force estimation and disturbance rejection: (1) Wind Tunnel Fan, (2) Wind-wall, (3) tethered payload, and (4) MAV with re-configurable arms. For all the cases mentioned above, the results demonstrated a significantly improved performance between the tests where the proposed NMHE module was enabled. More specific, for the *Wind Tunnel Fan* the MAV managed to maintain its position even when the air-speed reached to 7.5 m/s,

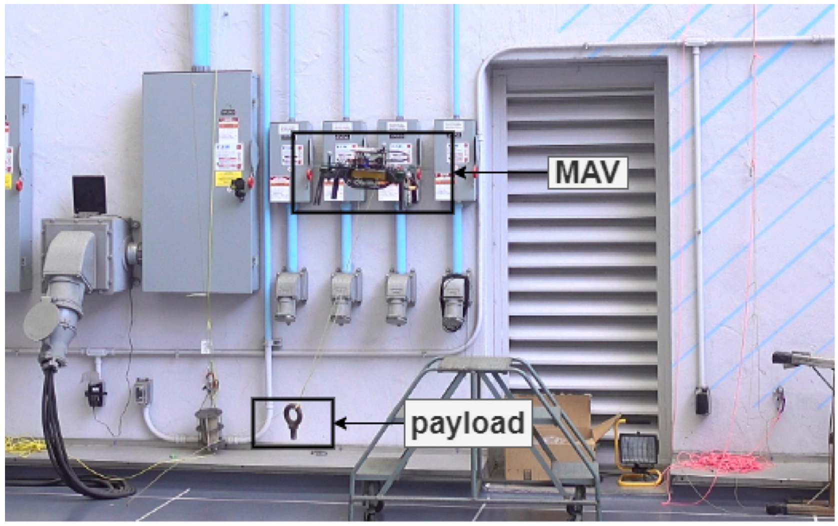

Fig. 19. Photographic still of the experimental scenario where the MAV has a tethered payload.

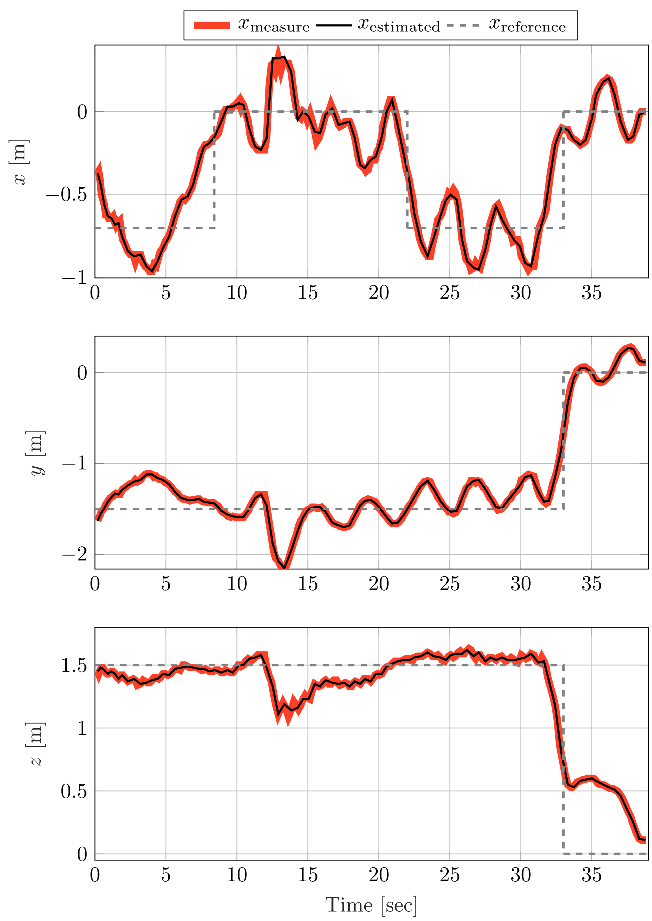

Fig. 20. Position states $[x, y, z]^{\top}$ of the scenario where a payload is attached on the MAV. The measured, estimated and reference values are shown by red, black, and dashed gray lines, respectively.

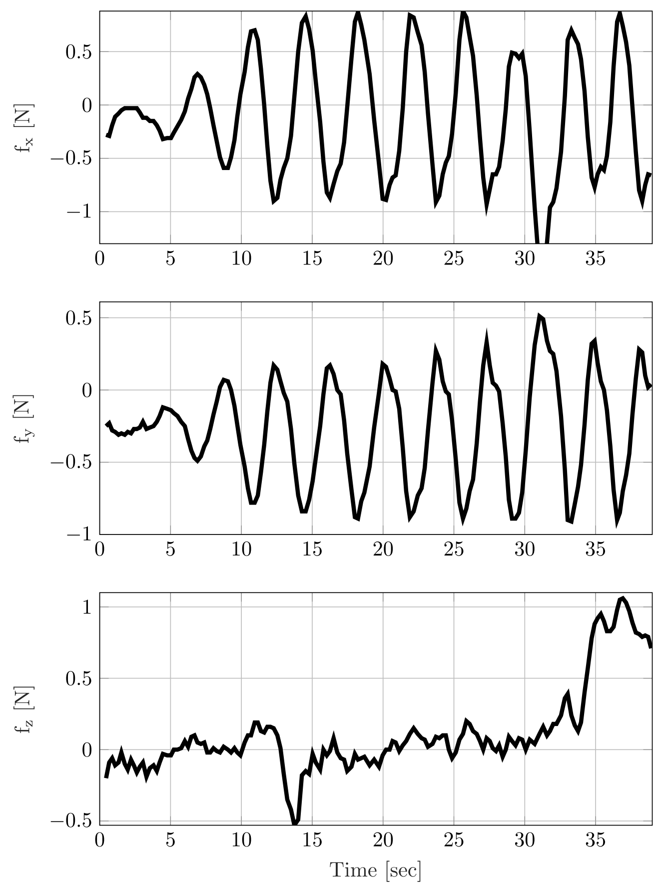

Fig. 21. Estimated forces $[f_x, f_y, f_z]^{\top}$, for the scenario where a payload is attached on the MAV.

while without external force estimation, the MAV failed to maintain its position at the lowest fan setting. Similar performance was observed during the evaluation under the effect of winds generated by a wind-wall. As far as the evaluation with a tethered payload is concerned, the proposed methodology estimates the increasing forces and compensates for them. Finally, the NMHE and NMPC modules identified the center of gravity variations due to the non-symmetric configurations of the re-configurable MAV as forces and compensated for them. On the other hand, when the NMHE module was suspended, the re-configurable

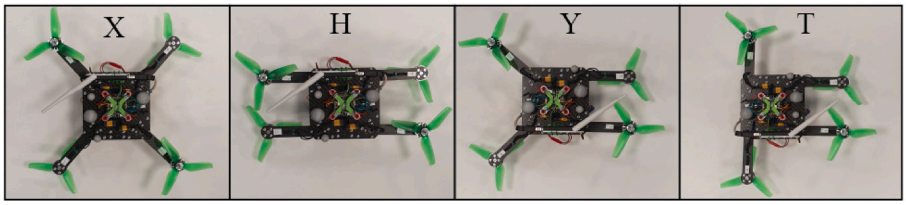

Fig. 22. Different formations *X*, *H*, *Y*, and *T* based on re-configurable MAV's arms position.

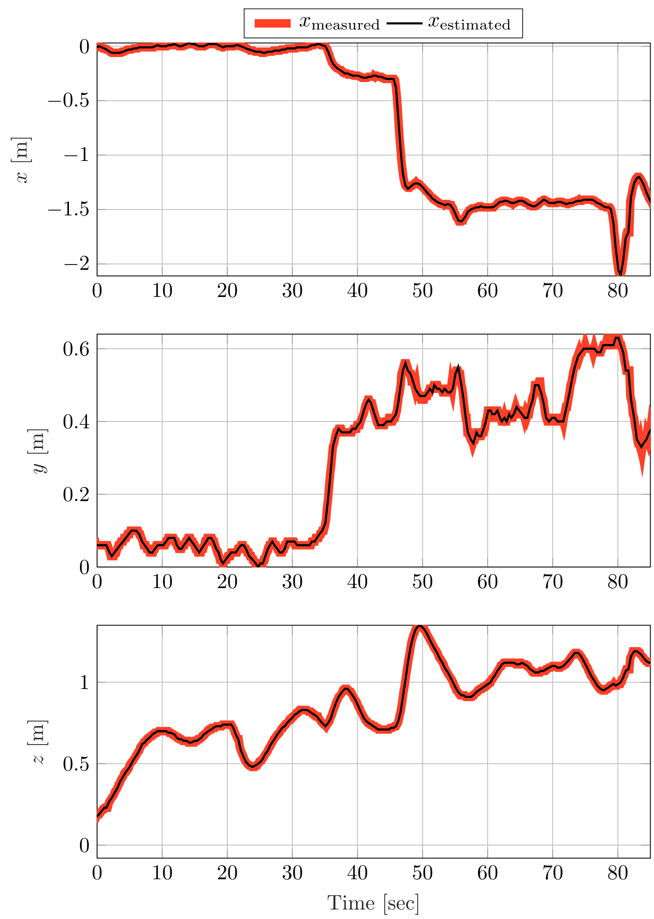

Fig. 23. Position states $[x, y, z]^{\top}$ of the experimental evaluation with the re-configurable MAV. The measured and estimated values are shown by red and black colors, respectively.

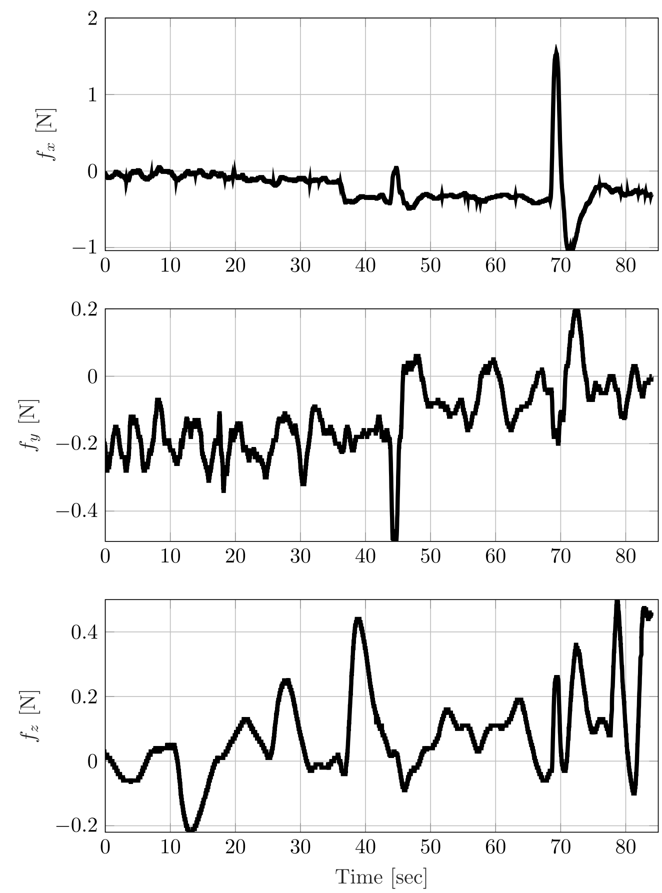

Fig. 24. Estimated forces $[f_x, f_y, f_z]^{\top}$, for the experimental evaluation of the proposed methodology with the re-configurable MAV.

MAV did not manage to regulate its position, and the flight resulted in a collision with the protection net.

CRediT authorship contribution statement

Andreas Papadimitriou: Conceptualization, Methodology, Software, Validation, Investigation, Writing – original draft, Writing – review & editing. **Hedyeh Jafari:** Conceptualization, Methodology, Investigation, Resources. **Sina Sharif Mansouri:** Conceptualization, Methodology, Software, Validation, Investigation, Writing – original draft, Writing – review & editing, Supervision. **George Nikolakopoulos:** Resources, Writing – original draft, Writing – review & editing, Project administration.

Declaration of competing interest

The authors declare that they have no known competing financial interests or personal relationships that could have appeared to influence the work reported in this paper.

Acknowledgments

We would like to thank, Center for Autonomous Systems and Technologies (CAST) at the California Institute of Technology, which gave us the opportunity to evaluate the proposed methods in their facilities. Our special thanks to Prof. Joel W. Burdick for providing access and Daniel Pastor for assisting in performing experiment evaluation at CAST.

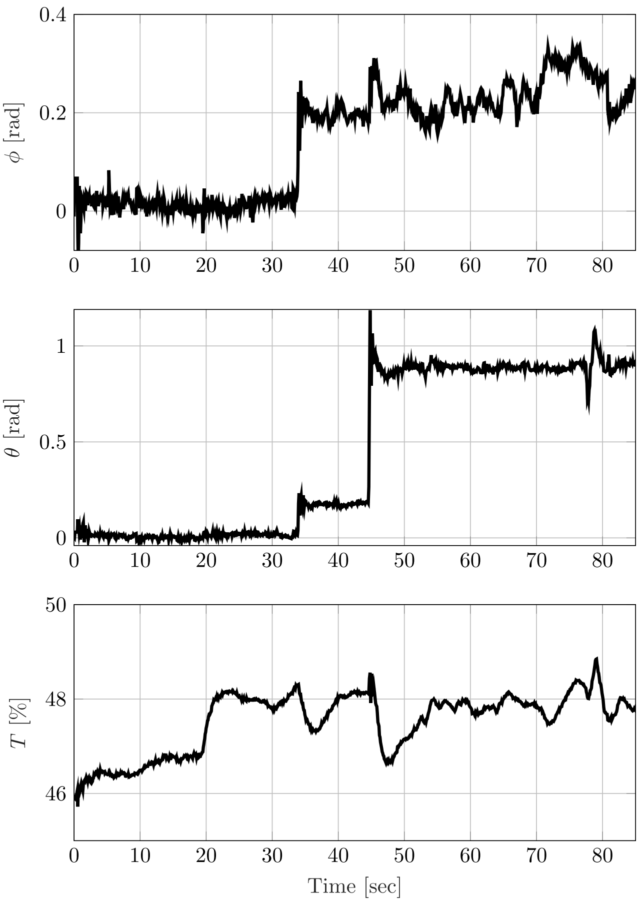

Fig. 25. Thrust, roll, and pitch commands generated by the NMPC for the experimental evaluation of the proposed methodology with the re-configurable MAV.

References

Abualigah, L., Yousri, D., Abd Elaziz, M., Ewees, A. A., Al-qaness, M. A., & Gandomi, A. H. (2021). Aquila optimizer: A novel meta-heuristic optimization algorithm. *Computers & Industrial Engineering*, *157*, Article 107250.

Abualigah, L. M. Q., et al. (2019). *Feature selection and enhanced Krill Herd algorithm for text document clustering*. Springer.

Andersson, J. A., Gillis, J., Horn, G., Rawlings, J. B., & Diehl, M. (2019). CasADi: a software framework for nonlinear optimization and optimal control. *Mathematical Programming Computation*, *11*(1), 1–36.

Belcastro, C. M., Newman, R. L., Evans, J., Klyde, D. H., Barr, L. C., & Ancel, E. (2017). Hazards identification and analysis for unmanned aircraft system operations. In *17th AIAA aviation technology, integration, and operations conference* (p. 3269).

Cho, A., Kim, J., Lee, S., & Kee, C. (2011). Wind estimation and airspeed calibration using a UAV with a single-antenna GPS receiver and pitot tube. *IEEE Transactions on Aerospace and Electronic Systems*, *47*(1), 109–117.

Davis, L. (1991). *VNR computer library*, *Handbook of genetic algorithms*. New York: Van Nostrand Reinhold.

Dunn, J. C., & Bertsekas, D. P. (1989). Efficient dynamic programming implementations of Newton's method for unconstrained optimal control problems. *Journal of Optimization Theory and Applications*, *63*(1), 23–38.

Falanga, D., Kleber, K., Mintchev, S., Floreano, D., & Scaramuzza, D. (2019). The foldable drone: A morphing quadrotor that can squeeze and fly. *IEEE Robotics and Automation Letters*, *4*(2), 209–216.

Fresk, E., & Nikolakopoulos, G. (2013). Full quaternion based attitude control for a quadrotor. In *2013 European control conference* (pp. 3864–3869). IEEE.

Haseltine, E. L., & Rawlings, J. B. (2005). Critical evaluation of extended Kalman filtering and moving-horizon estimation. *Industrial and Engineering Chemistry Research*, *44*(8), 2451–2460.

Hentzen, D., Stastny, T., Siegwart, R., & Brockers, R. (2019). Disturbance estimation and rejection for high-precision multirotor position control. In *2019 IEEE/RSJ international conference on intelligent robots and systems* (pp. 2797–2804).

Hollenbeck, D., Nunez, G., Christensen, L. E., & Chen, Y. (2018). Wind measurement and estimation with small unmanned aerial systems (suas) using on-board mini ultrasonic anemometers. In *2018 International conference on unmanned aircraft systems* (pp. 285–292). IEEE.

Jackson, J., Ellingson, G., & McLain, T. (2016). ROSflight: A lightweight, inexpensive MAV research and development tool. In *2016 International conference on unmanned aircraft systems* (pp. 758–762).

Kamel, M., Stastny, T., Alexis, K., & Siegwart, R. (2017). Model predictive control for trajectory tracking of unmanned aerial vehicles using robot operating system. In *Robot operating system (ROS)* (pp. 3–39). Springer.

Kan, X., Thomas, J., Teng, H., Tanner, H., Kumar, V., & Karydis, K. (2019). Analysis of ground effect for small-scale UAVs in forward flight. *IEEE Robotics and Automation Letters*, *4*, 3860–3867.

Kennedy, J. F., Kennedy, J., Eberhart, R. C., & Shi, Y. (2001). *Swarm intelligence*. Morgan Kaufmann.

Kocer, B. B., Tiryaki, M. E., Pratama, M., Tjahjowidodo, T., & Seet, G. G. L. (2019). Aerial robot control in close proximity to ceiling: A force estimation-based nonlinear MPC. In *2019 IEEE/RSJ international conference on intelligent robots and systems* (pp. 2813–2819).

Kominiak, D., Mansouri, S. S., Kanellakis, C., & Nikolakopoulos, G. (2020). MAV development towards navigation in unknown and dark mining tunnels. In *2020 28th Mediterranean conference on control and automation* (pp. 1015–1020). IEEE.

Kuře, M., Bušek, J., Vyhlídal, T., & Niculescu, S.-I. (2019). Damping oscillation of suspended payload by up and down motion of the pivot base - time delay algorithms for UAV applications. *IFAC-PapersOnLine*, *52*(18), 121–126, 15th IFAC Workshop on Time Delay Systems TDS 2019.

López-Negrete, R., Patwardhan, S. C., & Biegler, L. T. (2011). Constrained particle filter approach to approximate the arrival cost in moving horizon estimation. *Journal of Process Control*, *21*(6), 909–919.

Mansouri, S. S., Kanellakis, C., Fresk, E., Kominiak, D., & Nikolakopoulos, G. (2018). Cooperative coverage path planning for visual inspection. *Control Engineering Practice*, *74*, 118–131.

Mansouri, S. S., Kanellakis, C., Georgoulas, G., Kominiak, D., Gustafsson, T., & Nikolakopoulos, G. (2018). 2D visual area coverage and path planning coupled with camera footprints. *Control Engineering Practice*, *75*, 1–16.

Mansouri, S. S., Kanellakis, C., Kominiak, D., & Nikolakopoulos, G. (2020). Deploying MAVs for autonomous navigation in dark underground mine environments. *Robotics and Autonomous Systems*.

Mansouri, S. S., Kanellakis, C., Lindqvist, B., Pourkamali-Anaraki, F., Agha-Mohammadi, A.-A., Burdick, J., et al. (2020). A unified nmpc scheme for mavs navigation with 3d collision avoidance under position uncertainty. *IEEE Robotics and Automation Letters*, *5*(4), 5740–5747.

Mansouri, S. S., Karvelis, P., Kanellakis, C., Kominiak, D., & Nikolakopoulos, G. (2019). Vision-based mav navigation in underground mine using convolutional neural network. In *IECON 2019-45th annual conference of the IEEE industrial electronics society. vol. 1* (pp. 750–755). IEEE.

Marks, R. J. (1991). *Introduction to Shannon sampling and interpolation theory*. Berlin, Heidelberg: Springer-Verlag.

Neumann, P. P., & Bartholmai, M. (2015). Real-time wind estimation on a micro unmanned aerial vehicle using its inertial measurement unit. *Sensors and Actuators A: Physical*, *235*, 300–310.

Papadimitriou, A., Mansouri, S. S., Kanellakis, C., & Nikolakopoulos, G. (2021). Geometry aware NMPC scheme for morphing quadrotor navigation in restricted entrances. CoRR abs/2101.02965.

Peebles, P. Z. (2001). *Probability, random variables, and random signal principles, vol. 3*. McGraw-Hill New York.

Pereira, P. O., & Dimarogonas, D. V. (2019). Pose and position trajectory tracking for aerial transportation of a rod-like object. *Automatica*, *109*, Article 108547.

Quintero, S. A., Copp, D. A., & Hespanha, J. P. (2015). Robust UAV coordination for target tracking using output-feedback model predictive control with moving horizon estimation. In *2015 American control conference* (ACC), (pp. 3758–3764). IEEE.

Rao, C. V., & Rawlings, J. B. (2000). Nonlinear moving horizon state estimation. In *Nonlinear model predictive control* (pp. 45–69). Springer.

Rao, C. V., Rawlings, J. B., & Mayne, D. Q. (2003). Constrained state estimation for nonlinear discrete-time systems: Stability and moving horizon approximations. *IEEE Transactions on Automatic Control*, *48*(2), 246–258.

Rojas, R. (2010). Why the normal distribution. *Freis Universitat Berlin Lecture Notes*.

Sampedro, C., Rodriguez-Ramos, A., Bavle, H., Carrio, A., de la Puente, P., & Campoy, P. (2018). A fully-autonomous aerial robot for search and rescue applications in indoor environments using learning-based techniques. *Journal of Intelligent and Robotic Systems*, 1–27.

Sathya, A., Sopasakis, P., Van Parys, R., Themelis, A., Pipeleers, G., & Patrinos, P. (2018). Embedded nonlinear model predictive control for obstacle avoidance using PANOC. In *2018 European control conference* (pp. 1523–1528).

Siegwart, R., Nourbakhsh, I. R., & Scaramuzza, D. (2011). *Introduction to autonomous mobile robots* (pp. 265–275). MIT Press.

Sopasakis, P., Fresk, E., & Patrinos, P. (2020). OpEn: Code generation for embedded nonconvex optimization. arXiv, arXiv:2003.00292.

Sun, S., & de Visser, C. (2019). Aerodynamic model identification of a quadrotor subjected to rotor failures in the high-speed flight regime. *IEEE Robotics and Automation Letters*, *4*(4), 3868–3875.

Ungarala, S. (2009). Computing arrival cost parameters in moving horizon estimation using sampling based filters. *Journal of Process Control*, *19*(9), 1576–1588.

Wenz, A., & Johansen, T. A. (2017). Estimation of wind velocities and aerodynamic coefficients for uavs using standard autopilot sensors and a moving horizon estimator. In *2017 International conference on unmanned aircraft systems* (pp. 1267–1276). IEEE.

Wolf, C. A., Hardis, R. P., Woodrum, S. D., Galan, R. S., Wichelt, H. S., Metzger, M. C., et al. (2017). Wind data collection techniques on a multi-rotor platform. In *2017 Systems and information engineering design symposium* (pp. 32–37). IEEE.

Wuthier, D., Kominiak, D., Kanellakis, C., Andrikopoulos, G., Fumagalli, M., Schipper, G., et al. (2016). On the design, modeling and control of a novel compact aerial manipulator. In *Control and automation (MED), 2016 24th Mediterranean conference on* (pp. 665–670). IEEE.

Yang, X.-S. (2011). Metaheuristic optimization: algorithm analysis and open problems. In *International symposium on experimental algorithms* (pp. 21–32). Springer.